AGU PUBLICATIONS

Geophysical Research Letters

RESEARCH LETTER
10.1002/2015GL064715

Key Points:
- Apparent wave attenuation contains contributions from many source/sink terms
- Nonlinear energy transfer offsets the ice damping in storm cases significantly
- Frequency-dependent ice attenuation works the best in explaining field data

Correspondence to:
H. H. Shen,
hhshen@clarkson.edu

Citation:
Li, J., A. L. Kohout, and H. H. Shen (2015), Comparison of wave propagation through ice covers in calm and storm conditions, *Geophys. Res. Lett.*, *42*, 5935–5941, doi:10.1002/2015GL064715.

Received 27 MAY 2015
Accepted 23 JUN 2015
Accepted article online 25 JUN 2015
Published online 17 JUL 2015
Corrected 11 AUG 2015

This article was corrected on 11 AUG 2015. See the end of the full text for details.

Comparison of wave propagation through ice covers in calm and storm conditions

Jingkai Li[1,2], Alison L. Kohout[3], and Hayley H. Shen[2]

[1]Physical Oceanography Laboratory, Ocean University of China, Qingdao, China, [2]Department of Civil and Environmental Engineering, Clarkson University, Potsdam, New York, USA, [3]National Institute of Water and Atmospheric Research, Christchurch, New Zealand

Abstract Motivated by a dramatic reduction in Arctic sea ice cover, interest in the field of wave-ice interaction has accelerated over the past few years. Recent observations have identified that large waves (>3 m) have a linear attenuation rate, rather than the previously assumed exponential rate that is found for small waves. This suggests that waves penetrate further into the ice cover than previously expected. To explore this further we tested two exponentially decaying wave models. Contributions from nonlinear and wind generation source terms enabled both models to reproduce the observed regime shift. Essentially, the accumulation of nonlinear and wind energy contributions to long (and thus higher amplitude) waves can offset the ice damping, thus reducing the apparent attenuation. This study highlights the relevance of considering frequency dependence when analyzing wave attenuation in sea ice field data.

1. Introduction

Since the nineteenth century [*Greenhill*, 1886], wave propagation through ice-covered waters has been studied theoretically. The most recent review may be found in *Squire* [2007]. Motivated by the dramatic ice cover reduction in the Arctic, theoretical development has accelerated in the last 10 years. Although the total ice-covered area in the Antarctic has not reduced, regional variability has increased, most noticeably in the strong increase in the Ross Sea and the decrease in the Amundsen-Bellingshausen Sea [*Parkinson and Cavalieri*, 2012]. This regional variability has been shown to strongly correlate with wave climate change in the Southern Ocean [*Kohout et al.*, 2014]. Correlations between wind, wave, and ice cover retreat in the Arctic have also been obtained [*Thomson and Rogers*, 2014].

In contrast to the rich literature in wave-ice interaction theories, field data are extremely scarce. The most complete data set was obtained in the late 1970s and early 1980s as documented in *Wadhams et al.* [1986, 1988]. This situation will change in the near future, for several international field campaigns have recently been completed and more will take place soon.

One of the key questions concerning wave-ice interaction is the ability of an ice-covered ocean to attenuate wave energy. Nearly all theories demonstrate an exponential attenuation over distance. By adopting scattering as the underlying mechanism, the exponential coefficient was determined for a large set of observations made in the Bering and Greenland Seas. The exponential attenuation worked well except that a "rollover" phenomenon was found, such that as the wave period decreased the attenuation increased up to a point, beyond which the opposite happened [*Wadhams et al.*, 1988]. This phenomenon was speculated as resulting from the in situ wind-wave generation and cascade of energy from long to short waves. *Masson and Leblond* [1989] showed that the wind-wave generation in ice-covered water could be significant, while the nonlinear transfer from short to long waves was negligible.

With a new generation of wave buoy and data collection technology, *Kohout et al.* [2014] were able to obtain a long record of wave condition well within an ice cover. Their unprecedented data set covered both calm and storm periods. The most striking phenomenon from their data was the apparent wave attenuation as a function of the significant wave height H_s. At low wave heights, i.e., calm conditions, the apparent wave decay over distance $-\frac{dH_s}{dx}$ was proportional to H_s, indicating that $H_s \sim e^{-\alpha x}$. However, under storm conditions,

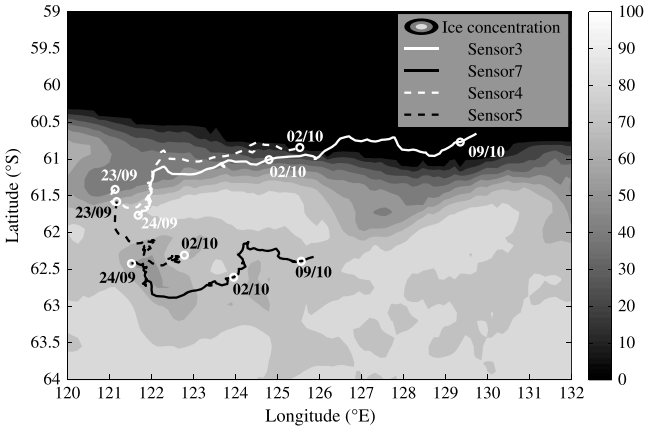

Figure 1. Locations and tracks of four wave sensors with average ice concentration between 23 September and 10 October 2012 (white represents 100% concentration, and black represents open water).

or large H_s, $-\frac{dH_s}{dx}$ became independent of H_s, indicating a linear attenuation with distance. By averaging the full data set, i.e., not separating the calm and large wave events, *Meylan et al.* [2014] focused on the exponential attenuation rates of the spectral components of the wavefield. They found a monotonic decrease of the attenuation with increasing wave period. Understanding of the attenuation of the spectral components during large wave events, however, remains unclear.

For large wave heights, the change of attenuation from exponential to linear suggests longer penetration of waves into an ice cover than implied by most of the theories. In this study, we follow *Masson and Leblond* [1989] to investigate all source terms in the spectral wave energy equation. We try to reconstruct the wave event that took place at the buoys reported in *Kohout et al.* [2014], in order to investigate the possible causes of the different wave attenuation between calm and stormy cases. To do so, we use WAVEWATCH III® v4.18 [*Tolman and WAVEWATCH III® Development Group*, 2014] (WW3) which provides several model options for ice-covered regions.

2. The Data Set

Kohout et al. [2014] reported the measurement of waves using simultaneous observations across hundreds of kilometers in the Antarctic marginal ice zone. Five sensors were deployed on sea ice between 60.5°S and 63°S on 23 and 24 September 2012. All times in the study are referenced to UTC. One of the sensors was lost during the first storm event. Deployment locations and tracks of four other wave sensors used in this study are shown in Figure 1. The data and details of this field experiment may also be found in *Kohout and Williams* [2013] and *Kohout et al.* [2015].

3. Hindcast of the Wavefield

To set up the hindcast, environmental forcing data need to be obtained. Sea surface wind and ice thickness data are from Climate Forecast System version 2 (CFSv2) Selected Hourly Time-Series Products of The National Centers for Environmental Prediction [*Saha et al.*, 2011]. The spatial resolution is longitudinally 0.205° and latitudinally 0.204°. The time resolution is 3 h. As the original thickness values of CFSv2 are usually larger than the real ice thicknesses in the field, the ice thickness data have been modified (scaled by 0.6) based on the observations. Ice thickness was estimated from shipboard observations to be between 0.5 and 1 m thick [*Kohout et al.*, 2014]. Daily average sea ice concentration is obtained from Artist Sea Ice-Special Sensor Microwave Imager [*Kaleschke and Kern*, 2006].

WW3 computes the evolution of wave action density $N = N(t, x, y, k, \theta)$ as a function of time t, space x and y, wave number k, and direction θ. The evolution of N is governed by

$$\frac{\partial N}{\partial t} + \frac{\partial}{\partial x}(C_{g,x}N) + \frac{\partial}{\partial y}(C_{g,y}N) + \frac{\partial}{\partial k}(C_k N) + \frac{\partial}{\partial \theta}(C_\theta N) = \boldsymbol{S}_{\mathrm{In}} + \boldsymbol{S}_{\mathrm{in}} + \boldsymbol{S}_{\mathrm{nl}} + \boldsymbol{S}_{\mathrm{ds}} + \boldsymbol{S}_{\mathrm{bot}} + \boldsymbol{S}_{\mathrm{db}} + \boldsymbol{S}_{\mathrm{tr}} + \boldsymbol{S}_{\mathrm{sc}} + \boldsymbol{S}_{\mathrm{ice}} + \boldsymbol{S}_{\mathrm{ref}}. \quad (1)$$

Among these source terms, linear input term $\boldsymbol{S}_{\mathrm{In}}$ relates to model initialization. Waves at sensor locations are all deepwater cases; therefore, the wave-bottom interaction $\boldsymbol{S}_{\mathrm{bot}}$, depth-induced breaking $\boldsymbol{S}_{\mathrm{db}}$, bottom scattering $\boldsymbol{S}_{\mathrm{sc}}$, and triad wave-wave interaction $\boldsymbol{S}_{\mathrm{tr}}$ are not considered here. For simplicity, reflections $\boldsymbol{S}_{\mathrm{ref}}$ by shorelines and icebergs are omitted too. We adopt the *Tolman and Chalikov*'s [1996]

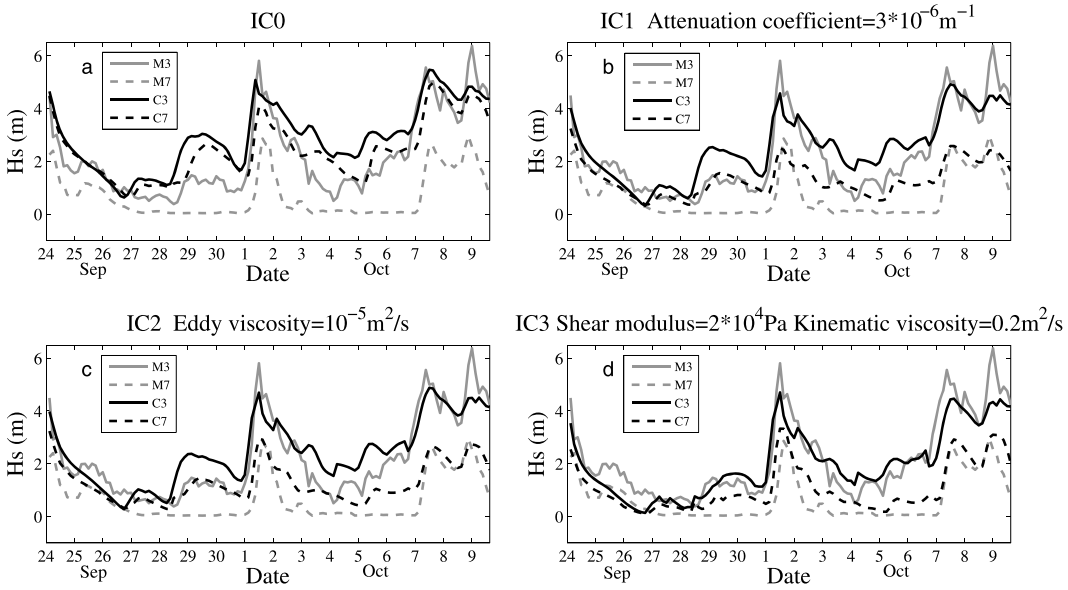

Figure 2. (a–d) Comparisons of measured and simulated significant wave height H_s of the sensor closest to the ice edge (sensor 3, measured: solid gray, simulated: solid black) and the sensor farthest from the ice edge (sensor 7, measured: dash gray, simulated: dash black) with different ice damping methods.

source term package for input $\boldsymbol{S}_{\text{in}}$ and dissipation $\boldsymbol{S}_{\text{ds}}$ and select the discrete interaction approximation for the nonlinear interaction $\boldsymbol{S}_{\text{nl}}$.

In this study, we define (45°S–75°S, 100°E–150°E) as the computational domain. This domain is tested to be sufficiently large so that further increase of the size does not affect the wave condition at the experimental site. We use the ETOPO2 bathymetry data and a regularly spaced latitude-longitude grid with 0.25° grid spacing. The wave number spacing is determined by the frequency intervals $\sigma_{m+1} = 1.1\sigma_m$, $m = 0, 1, \ldots, 24$ with $\sigma_0 = 0.0418$ Hz. The wave direction spacing is 15°. Four time steps are used in WW3 to reach computational efficiency: (a) a global time step (600 s) for the propagation of the entire solution, (b) a spatial time step (300 s) representing the spatial propagation, (c) a spectral time step (300 s) for intraspectral propagation, and (d) a source time step (100 s) for the source term integration.

For ice-covered regions, four models for $\boldsymbol{S}_{\text{ice}}$, IC0, IC1, IC2, and IC3, are tested and compared. The first one, IC0, treats ice covers as partial islands [*Tolman*, 2003], where wave energy is not damped, but its energy flux is partially blocked according to ice concentration. Another three models use different damping methods for the ice cover as described in the WW3 manual [*Tolman and WAVEWATCH III® Development Group*, 2014]. IC1 uses constant attenuation for all wave components. IC2 assumes that all damping comes from eddy viscosity in the boundary layer below the ice cover [*Liu and Mollo-Christensen*, 1988]. IC3 assumes that ice covers may be represented by a viscoelastic continuum [*Wang and Shen*, 2010]. In each case, WW3 calculates the complex wave number $k = k_r + ik_i$, with the real part k_r representing that the physical wave number related to wave phase speed and the imaginary part k_i to the exponential attenuation coefficient. Ice concentration is used to scale the other source terms. Formulations of other source terms are fixed in this study.

4. Results

To compare WW3 simulation results with the buoy data, two sensors with farthest distance travelled and longest time coverage are used. One is near the ice edge (sensor 3), and the other is more than 100 km away from the ice edge (sensor 7).

Comparisons between simulations and measurements of four different $\boldsymbol{S}_{\text{ice}}$ models are shown in Figure 2. For IC1, IC2, and IC3, many different input parameter values have been tested. The values that produced the least variance between simulated H_s and measured H_s over the duration of the field experiment are presented here. Regardless of the different ice models, simulated significant wave heights H_s are qualitatively consistent

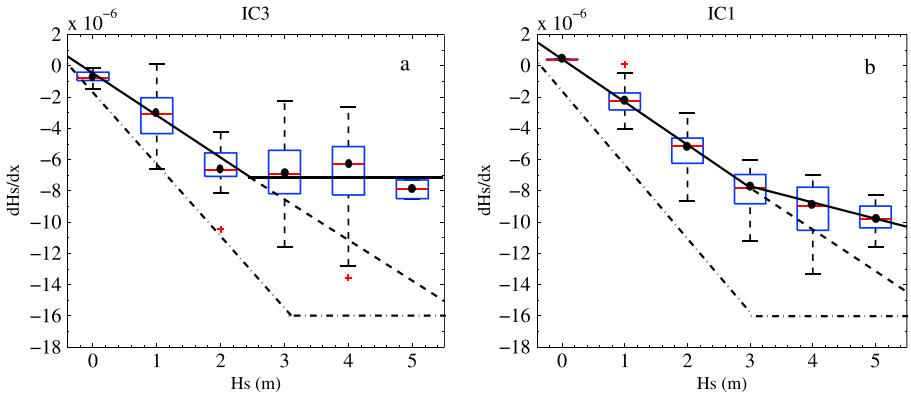

Figure 3. Decay rates of sensors farther than 100 km from the ice edge calculated by WW3 with (a) IC3 and (b) IC1. As was done in Figure 2 of *Kohout et al.* [2014], the black dot is the median, box height shows the range within which 50% of the data lie. The whiskers give the range of data, excluding outliers (crosses). The solid line is calculated from linear least squares regression through the median values. The dashed line shows the decay that would be expected if small-amplitude wave theory held for large waves. The dash-dotted line is the median value of the observed dH_s/dx.

with observations in both calm and storm cases, but there are some differences. For example, simulated peak H_s values are lower than field measurements. For IC0, simulated H_s further inside the ice cover (sensor 7) is always significantly higher than the measured data. Near the ice edge (sensor 3), simulated H_s is also distinctly larger than measurements but only in calm cases. For IC1 and IC2 the comparison improves, especially for the sensor further inside the ice cover. However, the simulated H_s is still too high in calm cases. By increasing the attenuation coefficient in IC1 or the eddy viscosity in IC2, the simulated H_s at both sensor locations drops for both calm and storm cases. Thus, comparison for calm cases would improve at the expense of storm cases, with an increase of total variance between the simulation and measurement. Conversely, by decreasing the attenuation coefficient in IC1 or the eddy viscosity in IC2, the opposite happens with an overall poorer comparison. The results shown in Figure 2 thus represent the best of the parameter values we tested.

To have a quantitative comparison among the four ice model results, we define the normalized root-mean-square error (NRMSE) between measured and simulated data as $\sqrt{\sum\left(\frac{X_c-X_m}{X_m}\right)^2/N}$, where X_c is the simulated H_s, X_m is the measured H_s, and N is the number of data points. Separating the storm and calm cases with a threshold of measured $H_s = 3$ m, we obtain the NRMSE of IC0, IC1, IC2, and IC3 to be 9.89, 4.74, 4.01, and 2.61, respectively, for the storm cases, and 20.56, 11.05, 9.94, and 5.74, respectively, for the calm cases. Of the four ice models, IC3 produces the least discrepancy between the measured data for both calm and storm cases, as the visual inspection of Figure 2 suggests.

5. Discussions

In *Kohout et al.* [2014], decay rate of the significant wave height, dH_s/dx, varies linearly with H_s until H_s reaches 3 m. When waves are larger than 3 m, dH_s/dx becomes independent of H_s. With IC3 results we examine the trend from simulated data as shown in Figure 3a. We interpolate the significant wave height H_s from WW3 at the location of each of the four sensors. Simulated time series from all four sensors were first calculated. To avoid noisy data, *Kohout et al.* [2014] focused on those data corresponding to sensor distances farther than 100 km from the ice edge to evaluate the trend of dH_s/dx. The same procedure is adopted here to calculate the decay of the significant wave height. As shown in Figure 3a, the magnitude of simulated dH_s/dx is smaller than the measured, as would be expected from comparing the calculated differences between sensors 3 and 7 with the measured differences in Figure 2d, but the trend is the same. The simulated result from IC1 shown in Figure 3b does not show the same qualitative behavior. This major difference between IC1 and IC3 is a consequence of their wave attenuation characteristics. While IC3 monotonically decreases the attenuation coefficient with increasing wave period [*Wang and Shen*, 2010], IC1 assumes that attenuation is constant across the entire wave spectrum. The monotonic wave attenuation with increasing period is clearly demonstrated in the present data set as shown in *Meylan et al.* [2014]. We will return to this phenomenon later.

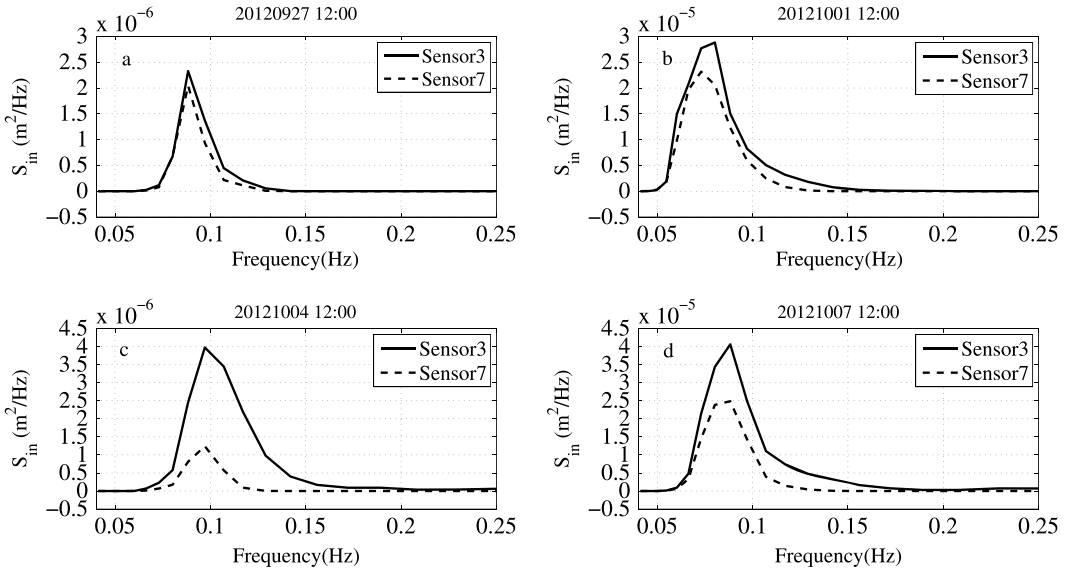

Figure 4. Source function of wind input term S_{in} at the locations of sensor 3 and sensor 7: (a and c) calm cases and (b and d) storm cases.

From Figure 2d, the simulated wave data using IC3 capture the time series behavior at both sensors 3 and 7 well; we thus use the calculated data to further analyze possible causes that lead to the change of apparent wave attenuation at high H_s. According to the discussion of equation (1) in Part 3, we then focus on wind input S_{in}, dissipation due to turbulence S_{ds}, nonlinear interaction S_{nl}, and ice damping S_{ice}. More details of these source terms are in the WW3 manual [*Tolman and WAVEWATCH III® Development Group*, 2014].

In the following analysis, we examine the simulated data for calm and storm cases separately. Based on H_s, two calm cases are randomly chosen on 27 September 2012 (20120927 in the figure titles) 12:00 and 04 October 2012 12:00. Two storm cases are chosen on 1 October 2012 12:00 and 7 October 2012 12:00. In all cases the waves were directed on ice. We integrate the source terms S_{in}, S_{nl}, and S_{ds} in all directions for these cases.

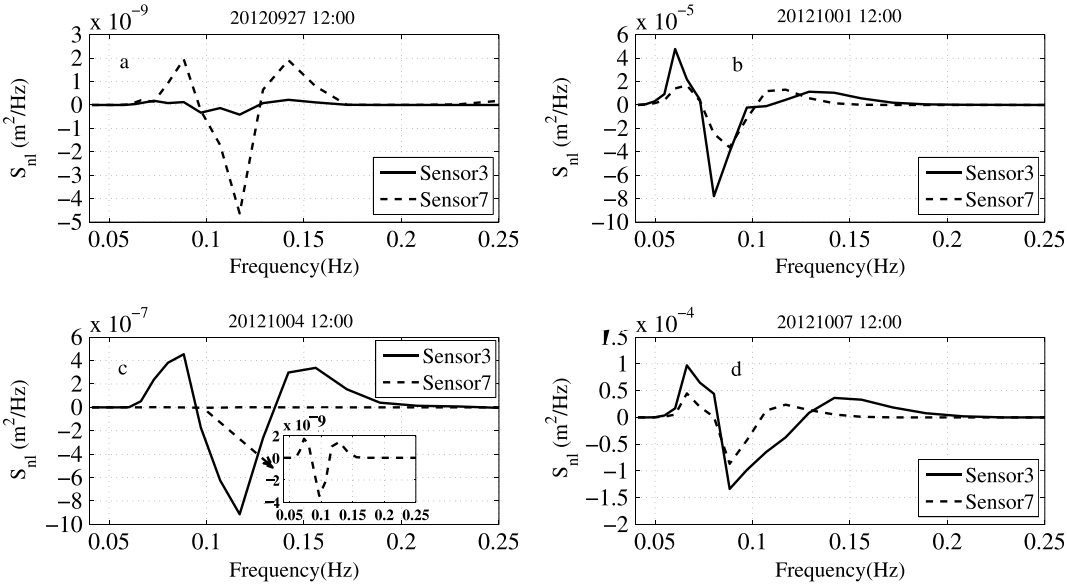

Figure 5. Source function of nonlinear interaction term S_{nl} at the locations of sensor 3 and sensor 7: (a and c) calm cases and (b and d) storm cases.

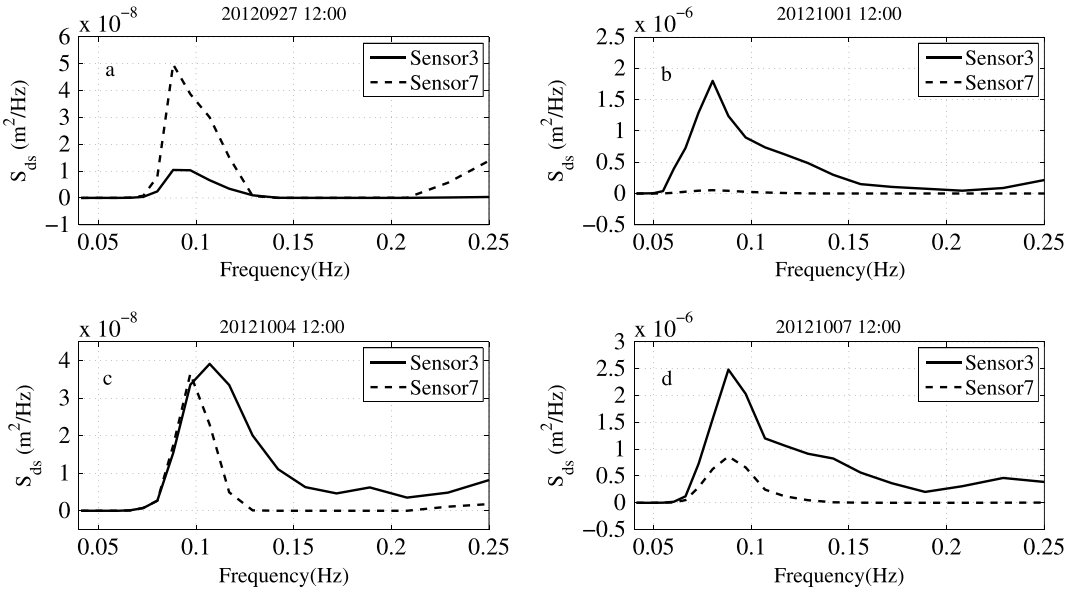

Figure 6. Source function of dissipation term $\boldsymbol{S}_{ds}$ at the locations of sensor 3 and sensor 7: (a and c) calm cases and (b and d) storm cases.

The integrated results $\int r(\sigma,\theta)d\theta$ at different locations of sensor 3 and sensor 7 are plotted in Figures 4–6, where $r(\sigma,\theta)$ is the source term value at frequency σ in the direction θ. Close attention should be paid to the substantial differences in the vertical scales between the calm and storm cases.

Figure 4 shows that in storm cases wind inputs more energy in all wave frequencies than in calm cases, as it should. The amounts of $\boldsymbol{S}_{in}$ in the calm cases are an order of magnitude less than in the storm cases. In addition, comparing the peak energy frequency between the calm and storm cases, wind energy input is much more productive in lower frequencies. Nonlinear wave interaction $\boldsymbol{S}_{nl}$ is shown in Figure 5, in which we observe that the dominant gain occurs at lower frequencies in the storm cases relative to the calm cases. Furthermore, compared with the storm cases, the amount of $\boldsymbol{S}_{nl}$ is negligible in the calm cases. Figure 6 shows that $\boldsymbol{S}_{ds}$ is an order of magnitude smaller than $\boldsymbol{S}_{nl}$ and $\boldsymbol{S}_{in}$ in storm cases. For calm cases, $\boldsymbol{S}_{ds}$ is comparable to $\boldsymbol{S}_{nl}$, both are negligible when compared with $\boldsymbol{S}_{in}$.

Thus, concerning the three source terms, wave turbulence dissipation may be ignored under the storm conditions. The nonlinear transfer process and the wind generation process put more wave energy into lower frequencies. Of the two, the nonlinear transfer process is a stronger effect in storm cases. Low-frequency long waves, which may grow to higher amplitude without breaking, may then be produced in storm cases. This mechanism contributes significantly to the less "apparent" attenuation observed in Figure 3a for H_s greater than 3 m.

To better understand the interaction of the different source terms, we return to Figure 3. For IC3, attenuation is sensitive to wave frequencies such that lower frequencies lead to smaller apparent attenuations even if we include other source terms. During storms, low-frequency waves grow higher while high-frequency waves break; hence, H_s increases with storms. For IC1, all frequencies are damped in the same way; hence, low-frequency waves do not have the same advantage of growing via the nonlinear contribution as in IC3. This explains why $-dH_s/dx$ is smaller for high H_s in IC3 relative to IC1.

6. Conclusion

We use hindcasts from WW3, with different settings for the sea ice, to reconstruct the wave conditions measured with buoys in a field experiment. This experiment covered both calm and storm conditions. We tested two wave damping models where both presume an exponential decay over distance. Both models show clear apparent change of attenuation between small and large waves. The model that damps high-frequency

waves more than low-frequency waves agrees better with the field data. From analyzing the other source terms, we believe that wind input and nonlinear interaction are both important in effecting the apparent attenuation. Accumulation of these energy contributions to long (and thus higher-amplitude) waves along the path of the propagation offsets the ice damping, thus reduces the apparent attenuation. WW3 currently treats the wind input, nonlinear interaction, and turbulent dissipation terms in partially ice-covered seas the same as in open water. The only adjustment is to multiply each term by the fraction of open water in ice-covered zones. In model applications herein, constant ice parameters (attenuation rate in the case of IC1; viscosity and elasticity in the case of IC3) are applied for the entire simulation, while the real ice cover is likely changing its properties both spatially and temporally. Discrepancies between the observation and the simulation may largely be the consequence of these simplifications. Nevertheless, from this first-order analysis, it is clear that in interpreting measured apparent wave attenuation we shall not ignore the contributions from other source terms.

Acknowledgments

The data used in this study are all provided in the references cited. The first author is a visiting doctoral student at Clarkson University. The financial support of China Scholarship Council and the hospitality of Clarkson University are appreciated. This work is supported in part by the Office of Naval Research grant N00014-13-1-0294, the Marsden Fund Council, administered by the Royal Society of New Zealand, NIWA through core funding under the National Climate Centre Climate Dynamics program. We thank Mike Williams and Erick Rogers for the comments on the manuscript.

The Editor thanks two anonymous reviewers for their assistance in evaluating this paper.

References

Greenhill, A. G. (1886), Wave motion in hydrodynamics, *Am. J. Math.*, *9*(1), 62–96, doi:10.2307/2369499.

Kaleschke, L., and S. Kern (2006), Sea-ice concentration for Arctic & Antarctic (ASI-SSMI), *Integrated Data Climate Center*. [Available at http://icdc.zmaw.de/seaiceconcentration_asi_ssmi.html.]

Kohout, A. L., and M. J. M. Williams (2013), *Waves-in-Ice Observations Made During the SIPEX II Voyage of the Aurora Australis, 2012*, Australian Antarctic Data Centre, Australia. [Available at http://dx.doi.org/10.4225/15/53266BEC9607F.]

Kohout, A. L., M. J. M. Williams, S. M. Dean, and M. H. Meylan (2014), Storm-induced sea-ice breakup and the implications for ice extent, *Nature*, *509*(7502), 604–607, doi:10.1038/nature13262.

Kohout, A. L., B. Penrose, S. Penrose, and M. J. M. Williams (2015), A device for measuring wave induced motion of ice floes in the Antarctic marginal ice zone, *Ann. Glaciol.*, *69*(59), doi:10.3189/2015AoG69A600.

Liu, A. K., and E. Mollo-Christensen (1988), Wave propagation in a solid ice pack, *J. Phys. Oceanogr.*, *18*(11), 1702–1712.

Masson, D., and P. H. Leblond (1989), Spectral evolution of wind-generated surface gravity waves in a dispersed ice field, *J. Fluid Mech.*, *202*, 43–81, doi:10.1017/S0022112089001096.

Meylan, M. H., L. G. Bennetts, and A. L. Kohout (2014), In situ measurements and analysis of ocean waves in the Antarctic marginal ice zone, *Geophys. Res. Lett.*, *41*, 5046–5051, doi:10.1002/2014GL060809.

Parkinson, C. L., and D. J. Cavalieri (2012), Antarctic sea ice variability and trends, 1979–2010, *Cryosphere*, *6*, 871–880, doi:10.5194/tc-6-871-2012.

Saha, S., et al. (2011), NCEP Climate Forecast System version 2 (CFSv2) Selected Hourly Time-Series Products, Tech. Rep., Research data archive at the *National Center for Atmospheric Research*, *Computational and Information Systems Laboratory*. [Available at http://rda.ucar.edu/datasets/ds094.1/.]

Squire, V. A. (2007), Of ocean waves and sea-ice revisited, *Cold Reg. Sci. Technol.*, *49*, 110–133.

Thomson, J., and W. E. Rogers (2014), Swell and sea in the emerging Arctic Ocean, *Geophy. Res. Lett.*, *41*, 3136–3140, doi:10.1002/2014GL059983.

Tolman, H. L. (2003), Treatment of unresolved islands and ice in wind wave models, *Ocean Model.*, *5*(3), 219–231, doi:10.1016/S1463-5003(02)00040-9.

Tolman, H. L., and D. V. Chalikov (1996), Source terms in a third-generation wind-wave model, *J. Phys. Oceanogr.*, *26*, 2497–2518.

Tolman, H. L., and the WAVEWATCH III® Development Group (2014), User manual and system documentation of WAVEWATCH III® version 4.18, NOAA Technical Note, MMAB Contribution No. 316, 311 p.

Wadhams, P., V. A. Squire, J. A. Ewing, and R. W. Pascal (1986), The effect of the marginal ice zone on the directional wave spectrum of the ocean, *J. Phys. Oceanogr.*, *16*(2), 358–376.

Wadhams, P., V. A. Squire, D. J. Goodman, A. M. Cowan, and S. C. Moore (1988), The attenuation rates of ocean waves in the marginal ice zone, *J. Geophys. Res.*, *93*(C6), 6799–6818, doi:10.1029/JC093iC06p06799.

Wang, R., and H. H. Shen (2010), Gravity waves propagating into an ice-covered ocean: A viscoelastic model, *J. Geophys. Res.*, *115*, C06024, doi:10.1029/2009JC005591.

Erratum

In the originally published version of this article, Clarkson University was listed twice as an affiliation, and the corresponding author was incorrect. The duplicated affiliation and the corresponding author have since been corrected, and this version may be considered the authoritative version of record.